Influence of boron vacancies on phase stability, bonding and structure of MB2 (M = Ti, Zr, Hf, V, Nb, Ta, Cr, Mo, W) with AlB2 type structure

Martin Dahlqvist, Ulf Jansson and Johanna Rosén

Original Publication:

Martin Dahlqvist, Ulf Jansson and Johanna Rosén, Influence of boron vacancies on phase stability, bonding and structure of MB2 (M = Ti, Zr, Hf, V, Nb, Ta, Cr, Mo, W) with AlB2 type structure, 2015, Journal of Physics: Condensed Matter, (27), 43, 435702.
http://dx.doi.org/10.1088/0953-8984/27/43/435702

Influence of boron vacancies on phase stability, bonding and structure of MB_2 (M = Ti, Zr, Hf, V, Nb, Ta, Cr, Mo, W) with AlB_2 type structure

Martin Dahlqvist[1*], Ulf Jansson[2], Johanna Rosen[1]

[1] Thin Film Physics Division, Department of Physics, Chemistry and Biology (IFM), Linköping University, SE-581 83 Linköping, Sweden.

[2] Department of Chemistry, The Ångström Laboratory, Uppsala University, Uppsala SE-751 21, Sweden

* Electronic mail: madah@ifm.liu.se

Transition metal diborides in hexagonal AlB_2 type structure typically form stable MB_2 phases for group IV elements (M = Ti, Zr, Hf). For group V (M = V, Nb, Ta) and group VI (M = Cr, Mo, W) the stability is reduced and an alternative rhombohedral MB_2 structure becomes more stable. In this work we investigate the effect of vacancies on the B-site in hexagonal MB_2 and its influence on the phase stability and the structure for TiB_2, ZrB_2, HfB_2, VB_2, NbB_2, TaB_2, CrB_2, MoB_2, and WB_2 using first-principles calculations. Selected phases are also analyzed with respect to electronic and bonding properties. We identify trends showing that MB_2 with M from group V and IV are stabilized when introducing B-vacancies, consistent with a decrease in the number of states at the Fermi level and by strengthening of the B-M interaction. The stabilization upon vacancy formation also increases when going from M in period 4 to period 6. For TiB_2, ZrB_2, and HfB_2, introduction of B-vacancies have a destabilizing effect due to occupation of B-B antibonding orbitals close to the Fermi level and an increase in states at the Fermi level.

1. Introduction

Transition metal borides exhibit an interesting combination of properties such as high hardness, low wear rate and excellent electrical conductivity, making them suitable for various thin film applications. A large number of boride phases with different crystal structures are known. One of the most common structure types is the hexagonal AlB_2 structure (P_6/mmm) typically formed by metal (M) constituents from groups IV through VI. This structure can be described as close-packed layers of the metal separated by planar layers of boron. The boron atoms form a honeycomb network with strong B-B bonds within the layer. The stability of the AlB_2 structure is dependent on the transition metal M. Typically, the group IV elements (Ti, Zr, Hf) form stable MB_2 phases with a limited homogeneity range. Going to group V (V, Nb, Ta) and group VI (Cr, Mo, W), the stability of the hexagonal MB_2 is reduced, and an alternative rhombohedral MB_2 structure ($R\bar{3}m$) with a puckered boron layer becomes more stable for transition metals in group VII and VIII. The reduced stability of the hexagonal MB_2 structure can be explained by trends in the electron structure. Analysis of the density of states (DOS) from density functional theory (DFT) calculations show a pseudogap separating bonding and antibonding M-d/B-p states [1, 2]. For the group IV transition metals, the Fermi level is positioned in the gap, filling all the bonding states. For the group V and VI elements, antibonding states are also filled, leading to a reduced stability of the structure. The stability can be affected by vacancies and other point defects. For example, it is well-known that the NbB_2 phase exhibits a homogeneity range of 65-70 at% B corresponding to a composition $NbB_{1.84}$ to $NbB_{2.34}$ [3]. Most likely, these vacancies are formed on both metallic and boron sites. Other metal diborides, however, such as CrB_2 exhibit no homogeneity range from the published phase diagrams [4].

Recently, we have observed that thin film synthesis from MB_2 (M = Nb, Cr, Mo) targets with a clear boron deficiency (B/M < 2) resulted in thin films exhibiting a B/M ratio ranging from 1.5 to 1.8 [5-7]. For the Cr-B and Mo-B systems, these compositions should lead to a mixture of phases including also more complex structures such as Cr_3B_4 and MoB. However, the phase analysis only showed the formation of substoichiometric hexagonal NbB_{2-x}, CrB_{2-x}, and MoB_{2-x}. The possibility to deposit highly substoichiometric MB_2 films by magnetron sputtering raises a number of questions regarding their stability and the effect of vacancies on the materials properties. No systematic study has yet been carried out to study the effect of vacancies on the AlB_2-type borides for the early transition metals. The aim with this work is therefore to use first-principles calculations to investigate how B-vacancy formation in hexagonal MB_2 (M = Ti, Zr, Hf, V, Nb, Ta, Cr, Mo, W) affects the stability and structure, and for selected compositions

also electronic structure. A comparison of MB_2 phases with M from group IV (M = Ti, Zr, Hf), V (M = V, Nb, Ta), and VI (M = Cr, Mo, W) will illustrate trends in vacancy formation for increasing number of d-electrons, while a comparison of M from period 4 (M = Ti, V, Cr), 5 (M = Zr, Nb, Mo), and 6 (M = Hf, Ta, W)will show the trends in vacancy formation going from a 3d to a 4d to a 5d metal.

2. Computational details

B-vacancies in MB_2 are modeled with the special quasi-random structure (SQS) method [8] to mimic an ideal random alloys of B-vacancies on the B-sites. SQS supercells were generated from 4×4×3 unit cells of the AlB_2-prototype structure at various B-vacancy concentrations x by optimizing the Warren-Cowley pair short-range order parameters [9, 10] up to the 8th shell. In total there are 48 M-sites at Wyckoff site 1a and 96 B-sites at Wyckoff site 2d, and Table I summarizes information for the supercells used to model MB_{2-x}. Figure 1(a) shows a supercell of MB_{2-x} with x = 0.167. The size of the supercell, 4×4×3 unit cells, is needed to obtain converged energies and bulk modulus while smaller supercells only give qualitative accurate equilibrium volumes. In addition, different ordered B-vacancy structures using a 2×2×2 unit cells with 23 (x = 0.125), 22 (x = 0.25), 21 (x = 0.375), and 20 (x = 0.5) atoms per cell were considered. These are defined in Table II along with enumerated B atoms in Fig. 1(b).

Table 1. Data for MB_{2-x} supercell of size 4×4×3 unit cells (4a × 4a × 3c).

x	at% B	# M atoms	# B atoms	# total atoms
0.000	66.7	48	96	144
0.083	65.7	48	92	140
0.167	64.7	48	88	136
0.250	63.6	48	84	132
0.333	62.5	48	80	128
0.500	60.0	48	72	120

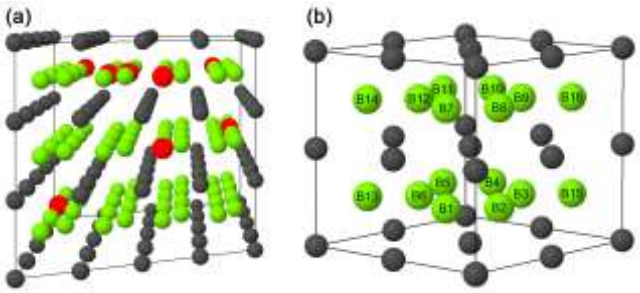

Figure 1. Schematic illustration of (a) a 4×4×3 SQS supercell used for modeling MB_{2-x} where x = 0.167, and (b) a 2×2×2 supercell, with enumerated B atoms, used for modeling ordered B-vacancies for x = 0.25 and 0.50. Red atoms represent B-vacancies, and M and B atoms are shown in black and green, respectively.

Table 2. List of ordered B-vacancies considered for MB_{2-x} where x = 0.125, 0.25, 0.375, and 0.5. The position of the B-vacancies are given by the numbers within parenthesis, which correspond to the enumeration of B-atoms in Fig. 1(b).

x	B-vacancy enumeration
0.125	(1)‡
0.25	(1, 2)‡, (1, 3), (1, 4), (1, 7), (1, 8), (1, 9)‡, (1, 10)
0.375	(1, 2, 8), (1, 2, 9), (1, 2, 10), (1, 3, 8), (1, 3, 9), (1, 3, 10), (1, 3, 11)‡, (1, 4, 7), (1, 4, 8)
0.5	(1, 2, 7, 8), (1, 2, 8, 9), (1, 2, 9, 10), (1, 2, 10, 11), (1, 3, 7, 9), (1, 3, 8, 10), (1, 3, 9, 11), (1, 3, 10, 12), (1, 4, 7, 10), (1, 4, 8, 11)

‡ Ordered structures used in Ref. [11].

All calculations are based on DFT within the generalized gradient approximation exchange-correlational functional as suggested by Perdew, Burke, and Ernzerhof (PBE) [12], using the projector augmented wave (PAW) technique [13] as implemented within VASP [14, 15]. We used a plane wave energy cutoff of 400 eV and the Monkhorst-Pack scheme [16] for integration of the Brillouin zone. For each considered phase the total energy is converged with respect to k-point sampling to within 0.2 meV/atom, e.g. for MB_{2-x} we used a 5×5×5 and 11×11×11 k-grids for 4×4×3 and 2×2×2 unit cells, respectively. Each phase was relaxed in terms of unit-cell volume, c/a ratio (when necessary), and internal atomic positions. Structures with disordered vacancies do break an initially assigned hexagonal crystal symmetry, though after complete relaxation there is no significant deviation from such complete symmetry. Since magnetism is beyond the scope of the present work, spin-polarization has been neglected throughout this study, although, e.g., CrB_2 has been shown to exhibit a helicoidal magnetic structure [17]. However, consideration of magnetism would only influence a potential quantification of calculated energies, and not the here investigated trends.

The chemical bonding was investigated in terms of projected crystal orbital Hamiltonian populations (pCOHP) which were derived using the LOBSTER program [18-20]. Using this method the calculated band-structure energy is reconstructed into orbital interactions. Positive

COHP values indicate an anti-bonding interaction, and negative COHP values indicate a bonding interaction. Bonding energies are obtained by integration of COHP up to the Fermi level (ICOHP).

3. Results and discussion

3.1. Stability of *M*B$_2$ with boron vacancies

In order to evaluate the stability of *M*B$_2$ upon introduction of B-vacancies, the energy of this phase needs to be compared to the energy of single elements and binary phases within the *M*-B system. Identification of these competing phases are based on experimental phase diagrams, e.g. see Ref. [21-24], and Table A1 and A2 encompass these including their calculated total energy and lattice parameters.

In a first comparison, we construct a 0 K "phase diagram" for the *M*-B binaries listed in Table AI and AII, using the binary formation energy ΔE_1 given by

$$\Delta E_1 = E\left[M_{1-y}\mathrm{B}_y\right] - (1-y)E[M] - yE[\mathrm{B}], \qquad (1)$$

where $E\left[M_{1-y}\mathrm{B}_y\right]$ is the energy of the binary phases per atom, and $E[M]$ and $E[\mathrm{B}]$ is the energy per atom of *M* and B in their low energy structures, respectively. ΔE_1 for all binaries are displayed in Fig. 2, where negative values of ΔE_1 implies that the binary compounds are energetically favored with respect to the lowest energy structures of *M* and B. From this plot, a simple construction known as convex hull can be made, which consists of data points forming a convex envelope. Phases present on this convex hull are the most stable phases or ground states in the system. Phases above the convex hull are not stable at 0 K. For comparison, the formation energy of hexagonal *M*B$_2$ are also included in Fig. 2, with *M* = Ti, Zr, Hf, V, Nb found to be part of the convex hull and therefore considered stable. However, for *M* = Ta, Cr, Mo, and W the rhombohedral MoB$_2$ ($R\bar{3}m$) or hexagonal WB$_2$ ($P6_3/mmc$) type-structures are lower in energy compared to the metastable hexagonal AlB$_2$ type-structure, though not clearly seen in inset of Fig. 2(f-i) due to a small energy difference. Hence the rhombohedral MoB$_2$ and WB$_2$ and hexagonal TaB$_2$ and CrB$_2$ belongs to the convex hull. Neither TiB$_2$, ZrB$_2$, nor HfB$_2$ gain any energy by forming B-vacancies, evident from the resulting phases being above the convex hull. This is consistent with reported phase diagrams where they are shown to be close

to line compounds [21, 22]. For group V, ΔE_1 increases for VB_{2-x} with increasing x while both NbB_{2-x} and TaB_{2-x} do show a decrease of ΔE_1 for $0 < x < 0.083$, corresponding to 66.7 – 65.7 at% B, and $0 < x < 0.25$, corresponding to 66.7 – 63.6 at% B, respectively. For group VI, ΔE_1 decreases up to x = 0.25, 0.333, and at least 0.5 for CrB_{2-x}, MoB_{2-x}, and WB_{2-x}, respectively. However, in this comparison (Fig. 2) we do only get information on the stability of MB_{2-x} relative to M and B. Therefore, we also have to compare to the phases that belongs to the convex hull, and identify the set of most competing phases, for further details see Refs. [25, 26] This approach has been shown effective for both verifying and predicting the existence of binary, ternary and quaternary compounds [26-28], and found valid also for temperatures T > 0 K [29].

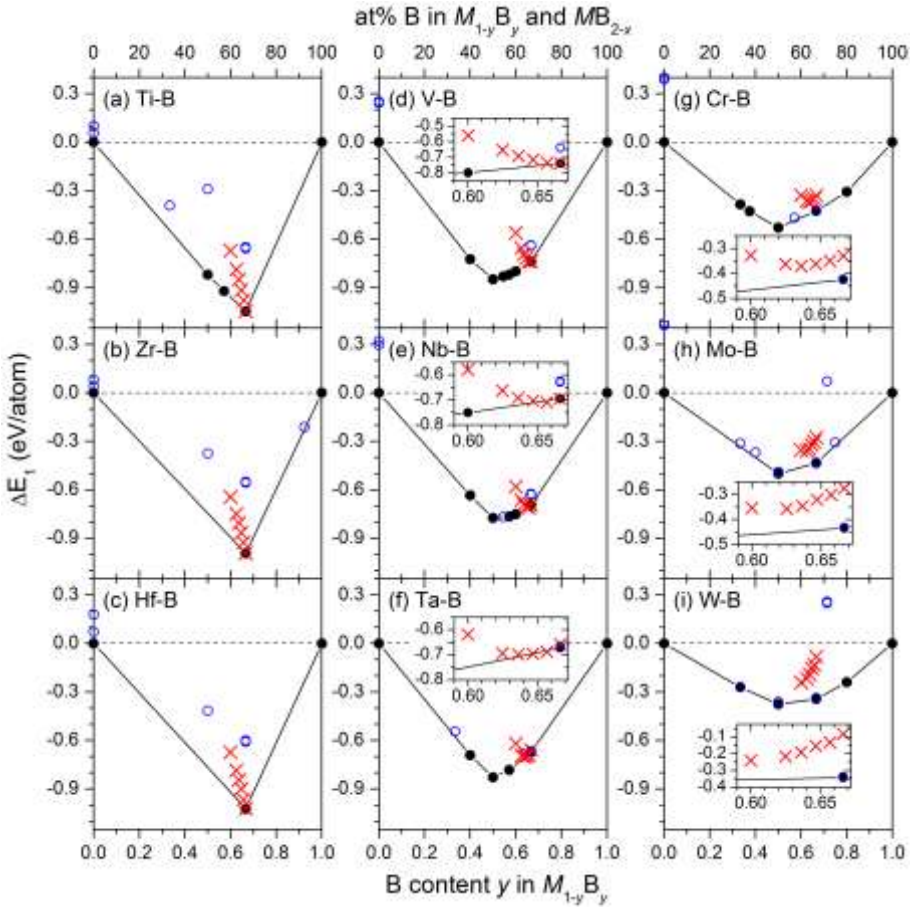

Figure 2. Formation energy ΔE_1 of $M_{1-y}B_y$ binary phases as a function of B concentration y for M = Ti, Zr, Hf, V, Nb, Ta, Cr, Mo, W using Eq. 1. The formation energy of the hexagonal AlB_2 type structure of MB_2 upon B-vacancy formation is represented by (×), with increasing vacancy concentration going to the left. Binary phases with $\Delta E_1 < 0$ are stable with respect to M and B. The black line represents the convex hull, excluding MB_{2-x} when $x \neq 0$. Phases which do not belong to the convex hull are represented by blue circles (○). See Table A2 for a complete list of competing phases.

The formation enthalpy of $M\mathrm{B}_{2-x}$ with respect to the set of most competing phases, at zero pressure, is calculated as

$$\Delta H_{\mathrm{cp}} = E[M\mathrm{B}_{2-x}] - E[\text{competing phases}], \qquad (2)$$

where $E[M\mathrm{B}_{2-x}]$ is the total energy for $M\mathrm{B}_{2-x}$ and $E[\text{competing phases}]$ the energy for the identified set of most competing phases at the $M\mathrm{B}_{2-x}$ composition. Corresponding free energy is approximated as

$$\Delta G_{\mathrm{cp}} = \Delta H_{\mathrm{cp}} - T\Delta S, \qquad (3)$$

where

$$\Delta S = -2k_B[z\ln(z) + (1-z)\ln(1-z)], \qquad (4)$$

per formula unit is the entropy of an ideal solution of B and B-vacancies on the boron sublattice. Notice that z is related to x as $z = x/2$. For illustrative purpose, ΔG_{cp} is presented for T = 1000 K in this work.

Table 3. Identified set of most competing phases for $M\mathrm{B}_{2-x}$, where M = Ti, Zr, Hf, V, Nb, Ta, Cr, Mo, W and $0 \leq x \leq 0.5$.

x	Set of most competing phases for $M\mathrm{B}_{2-x}$				
	Ti	Zr	Hf	V	Nb
0.000	TiB_2	ZrB_2	HfB_2	VB_2	NbB_2
0.083	TiB_2, Ti_3B_4	ZrB_2, Zr	HfB_2, Hf	VB_2, V_2B_3	NbB_2, Nb_2B_3
0.125	TiB_2, Ti_3B_4	ZrB_2, Zr	HfB_2, Hf	VB_2, V_2B_3	NbB_2, Nb_2B_3
0.167	TiB_2, Ti_3B_4	ZrB_2, Zr	HfB_2, Hf	VB_2, V_2B_3	NbB_2, Nb_2B_3
0.250	TiB_2, Ti_3B_4	ZrB_2, Zr	HfB_2, Hf	VB_2, V_2B_3	NbB_2, Nb_2B_3
0.333	TiB_2, Ti_3B_4	ZrB_2, Zr	HfB_2, Hf	VB_2, V_2B_3	NbB_2, Nb_2B_3
0.375	TiB_2, Ti_3B_4	ZrB_2, Zr	HfB_2, Hf	VB_2, V_2B_3	NbB_2, Nb_2B_3
0.500	TiB_2, Ti_3B_4	ZrB_2, Zr	HfB_2, Hf	V_2B_3	Nb_2B_3
x	Ta	Cr	Mo	W	
0.000	TaB_2($P6_3/mmc$)	CrB_2 ($P6_3/mmc$)	MoB_2 ($R\bar{3}m$)	WB_2 ($R\bar{3}m$)	
0.083	TaB_2($P6_3/mmc$), Ta_3B_4	CrB_2 ($P6_3/mmc$), CrB	MoB_2 ($R\bar{3}m$), MoB ($I4_1/amd$)	WB_2 ($R\bar{3}m$), WB ($14/m$)	
0.125	TaB_2($P6_3/mmc$), Ta_3B_4	CrB_2 ($P6_3/mmc$), CrB	MoB_2 ($R\bar{3}m$), MoB ($I4_1/amd$)	WB_2 ($R\bar{3}m$), WB ($14/m$)	
0.167	TaB_2($P6_3/mmc$), Ta_3B_4	CrB_2 ($P6_3/mmc$), CrB	MoB_2 ($R\bar{3}m$), MoB ($I4_1/amd$)	WB_2 ($R\bar{3}m$), WB ($14/m$)	
0.250	TaB_2($P6_3/mmc$), Ta_3B_4	CrB_2 ($P6_3/mmc$), CrB	MoB_2 ($R\bar{3}m$), MoB ($I4_1/amd$)	WB_2 ($R\bar{3}m$), WB ($14/m$)	
0.333	TaB_2($P6_3/mmc$), Ta_3B_4	CrB_2 ($P6_3/mmc$), CrB	MoB_2 ($R\bar{3}m$), MoB ($I4_1/amd$)	WB_2 ($R\bar{3}m$), WB ($14/m$)	

0.375	TaB_2($P6_3/mmc$), Ta_3B_4	CrB_2 ($P6_3/mmc$), CrB	MoB_2 ($R\bar{3}m$), MoB ($I4_1/amd$)	WB_2 ($R\bar{3}m$), WB
0.500	TaB_2($P6_3/mmc$), Ta_3B_4	CrB_2 ($P6_3/mmc$), CrB	MoB_2 ($R\bar{3}m$), MoB ($I4_1/amd$)	WB_2 ($R\bar{3}m$), WB

For systems with *M* = Ti, Zr, Hf, V, and Nb the AlB_2 type structure is found stable at $x = 0$ with ΔH_{cp} = -329, -435, -414, -73, and -69 meV/atom, respectively, and hence these phases are included as competing phases in respective system from here on. Table III shows the identified set of most competing phases for MB_{2-x}. Notice that for *M* = Ti, Zr, Hf, V, and Nb and $x \leq 0.375$, the hexagonal MB_2 is identified as part of the set of most competing phases. For *M* = Ta, Cr, Mo, W, the rhombohedral MoB_2 or hexagonal WB_2 type structures are identified as a most competing phase. Figure 3 shows the trends for ΔH_{cp} and ΔG_{cp} as function of the B-vacancy concentration *x*. *M* from group IV show a clear tendency of not forming B-vacancies as ΔH_{cp} and ΔG_{cp} increases with increasing number of B-vacancies. For group V, VB_{2-x} show similar trends in ΔH_{cp} as *M* from group IV although with a smaller increase at low x. NbB_{2-x} and TaB_{2-x} on the other hand displays a negative ΔH_{cp} for $x < 0.13$ and $0.06 < x < 0.17$, while at higher vacancy concentration the competing phases are energetically favored. However, with increased temperature, here exemplified at 1000 K, the range of *x* for which $\Delta G_{\mathrm{cp}} < 0$ is extended to higher vacancy concentration, $x < 0.23$ for NbB_{2-x} and $0.05 < x < 0.34$ for TaB_{2-x}. For group VI, ΔH_{cp} is positive for all *x*, though with decreasing energy for increasing vacancy concentration. This decrease is getting more pronounced when going from for CrB_{2-x} to WB_{2-x}.

If we look at the here considered ordered B-vacancy distributions most are found with $\Delta H_{\mathrm{cp}}^{\mathrm{order}} > 0$, see Fig. 3. The only exception is for NbB_{2-x} at $x = 0.125$ and TaB_{2-x} at x = 0.125 and 0.25. Common for energetically preferred ordered configurations for MB_{2-x} with *M* from group IV are nearest neighbor vacancy pairs within the B-layer, see e.g. (1, 2) and (1,2,7,8) in Table II and Fig. 1(b), whereas group V and VI show tendencies of B-vacancy formation in separate B-layers, see e.g. (1, 9) in Table II and Fig. 1(b). There is also a larger spread in $\Delta H_{\mathrm{cp}}^{\mathrm{order}}$ for group IV as compared to group V and VI, most ordered configurations are found with $\Delta H_{\mathrm{cp}}^{\mathrm{order}} < \Delta H_{\mathrm{cp}}^{\mathrm{disorder}}$. For some configurations $\Delta H_{\mathrm{cp}}^{\mathrm{order}} < \Delta G_{\mathrm{cp}}$ indicating tendency for ordered B-vacancies even at increase temperatures. We note that a previous study of ordered B-vacancies in MoB_2 show similar trends, with decreasing $\Delta H_{\mathrm{cp}}^{\mathrm{order}}$ as *x* increases, though with $\Delta H_{\mathrm{cp}}^{\mathrm{order}}$= -37 meV/atom at $x = 0.375$ [11]. Note that a different code, CPMD, was used in their study. At elevated temperatures, contributions to the free energy besides configurational

entropy might be taken into consideration. However, in similar hexagonal layered materials, vibrational and electronic contributions been shown to almost cancel out and hence not influence ΔG_{cp} significantly [29].

In addition, the formation energy $E_{\mathrm{vac}}^{\mathrm{f}}$ of a B monovacancy has been calculated using a 4×4×3 unit cell, from

$$E_{\mathrm{vac}}^{\mathrm{f}} = E_{\mathrm{vac}} - \frac{n-1}{n} E_{\mathrm{bulk}}, \qquad (5)$$

where E_{vac} is the total energy of the cell with one B-vacancy, n is the number of atoms in the bulk cell, and E_{bulk} the total energy for the bulk cell without a vacancy. The inset in Fig. 3(f) shows $E_{\mathrm{vac}}^{\mathrm{f}}$ as function of M in group VI, V, and VI. As the number of valence electrons increases $E_{\mathrm{vac}}^{\mathrm{f}}$ is decreasing. For M = Ti and Zr, positive values of $E_{\mathrm{vac}}^{\mathrm{f}}$ are found indicating a cost in energy to form a vacancy. This also clarifies why nearest neighbor vacancy pairs, i.e. a bivacancy, are favored for TiB_2 and ZrB_2. For example, 6 B-B bonds are broken if two isolated B-vacancies are formed while only 5 B-B bonds are broken if one bivacancy appears. However, MB_{2-x} for group V and VI has $-0.75 \leq E_{\mathrm{vac}}^{\mathrm{f}} \leq -3.76$ which indicates a gain in energy upon formation of B-vacancies. This also explains why isolated vacancies are preferred as more bonds are broken in comparison to bivacancy formation.

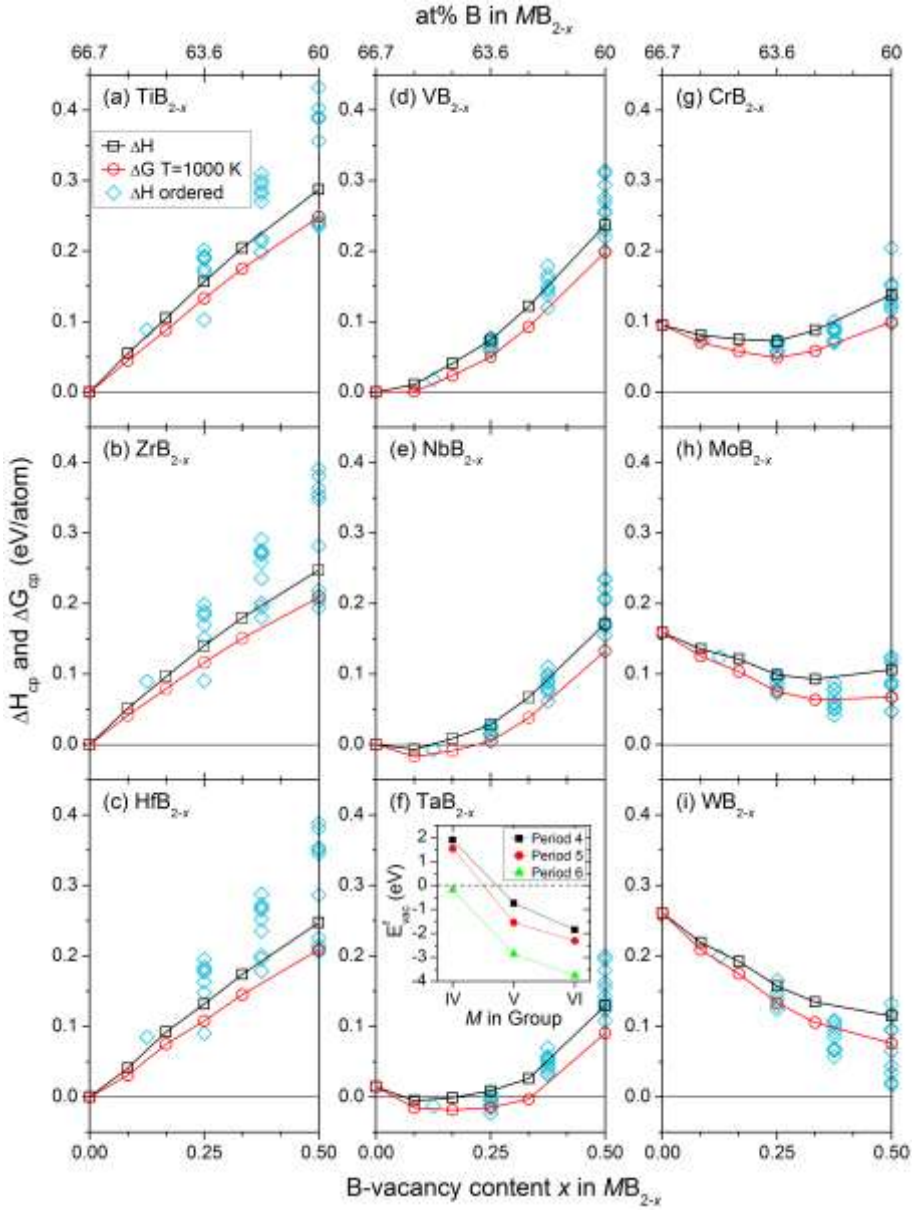

Figure 3. Formation enthalpy ΔH_{cp} of ordered (◊) and disordered (□) B-vacancies in $M\mathrm{B}_{2-x}$ as well as mean field free energy ΔG_{cp} at 1000 K (○) for a disordered vacancy distribution using Eq. 2 and 3, as a function of B-vacancy concentration x for M = Ti, Zr, Hf, V, Nb, Ta, Cr, Mo, W. Negative values indicate favored B-vacancy formation. ΔH_{cp} and ΔG_{cp} is calculated using Eq. 2 and 3, respectively. The inset in panel (d) shows the monovacancy formation energy $E^{\mathrm{f}}_{\mathrm{vac}}$ of B in $M\mathrm{B}_{2-x}$ as function of M in group VI, V, and VI.

3.2. Structural aspects of $M\mathrm{B}_{2-x}$

Figure 4 shows the calculated volume and lattice parameters a and c of the $M\mathrm{B}_{2-x}$ phases as a function of the amount of B-vacancies x. In terms of volume change relative to vacancy free

MB_2, the introduction of B-vacancies results in a volume decrease for all *M* but Zr and Hf for which a small but significant increase is found. Structurally, the lattice parameters of *M* from group IV show an increase in *a* and a decrease in *c* as the amount of B-vacancies increases. Reported values for VB_{2-x} at $x = 0$ are in excellent agreement with calculated ones. NbB_{2-x} and TaB_{2-x} shows a corresponding decrease in *c*, from 3.339 Å ($x = 0$) to 3.212 Å ($x = 0.5$) and from 3.327 Å ($x = 0$) to 3.197 Å ($x = 0.5$), respectively, while *a* is close to constant around 3.125 Å and 3.105 Å, respectively. This is in excellent agreement with experimentally reported substoichiometric NbB_{2-x} ($x = 0.2$), for which a = 3.12 Å and c = 3.28 Å [5] and TaB_{2-x} ($x = 0.19$), for which a = 3.097 Å and c = 3.242 Å [30]. For MoB_{2-x} and WB_{2-x}, *a* increases up to $x = 0.25$ after which it starts to decrease, whereas the c parameter decreases more rapidly in comparison to group IV and V. For substoichiometric MoB_{2-x} ($x = 0.4$), the calculated lattice parameters are in agreement with reported lattice parameters of $a = 3.05$ Å and $c = 3.07$ Å. For WB_{2-x}, similar lattice parameters have been reported, $a \sim 3.02$ and $c \sim 3.06$ Å, although for allegedly different compositions, $x = 0$ [31] and $x \sim 0.8$ [31]. Hence, the parameters are represented by green horizontal dashed lines in the interval $0.0 \leq x \leq 0.5$ in Fig. 4, which is close to the calculated values at $x = 0.5$. For CrB_{2-x}, the experimental structural parameters are larger than those calculated, which is expected since CrB_{2-x} has been treated as non-magnetic within this work.

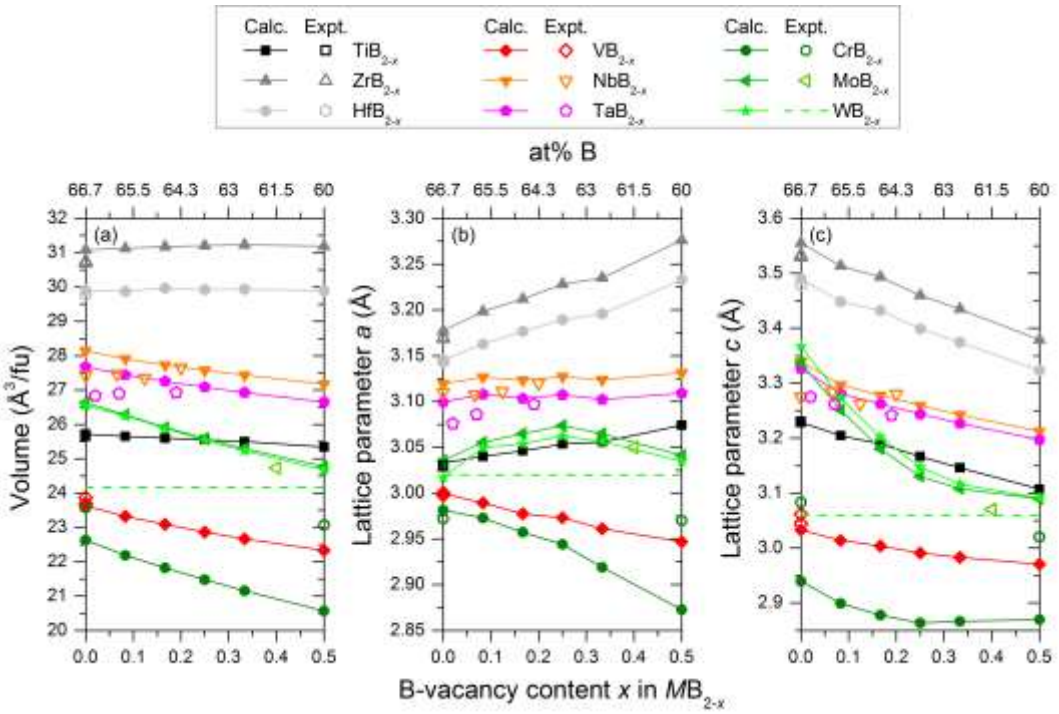

Figure 4. Calculated volume (a) and lattice parameters *a* (b) and *c* (c) as a function of B-vacancy concentration *x* in MB_{2-x} for *M* = Ti, Zr, Hf, V, Nb, Ta, Cr, Mo, W (filled symbols). For

comparison, experimental values are also displayed (open symbols, dashed green line for WB_{2-x} due to allegedly different compositions) [3, 5-7, 30-40].

The structure of MB_{2-x} (M = Ti, Zr, Nb, Mo) is further evaluated in Fig. 5, showing the average atomic distances of the in- and out-of-plane B-B and *M*-*M*, and of *M*-B, for the vacancy-free structure (x = 0) and for three selected B-vacancy concentrations (x = 0.167, 0.333 and 0.5). Note that *M*-B is a mix of an in- and out-of-plane distance. The trends for next nearest neighbor in-plane B-B and in-plane *M*-*M* clearly follows the lattice parameter a in Fig. 4, as do out-of plane B-B and *M*-*M* in comparison to the lattice parameter c. For TiB_{2-x} and ZrB_{2-x}, with M from same group but different periods, the nearest neighbor in-plane B-B show a small increase up to x = 0.167 after which it decreases. Such trends do not directly follow observed trends for the lattice parameter a. The *M*-B distance is almost constant with increasing x. This can be understood from the opposite trends of a and c in Fig.4 which results in small changes of the volume and hence for *M*-B. ZrB_{2-x}, NbB_{2-x}, and MoB_{2-x}, with M from the same period but different groups, display different nearest neighbor in-plane B-B trends with increasing x. Compared to ZrB_{2-x}, B-B is almost constant for NbB_{2-x} whereas a clear increase is seen for MoB_{2-x}. Corresponding *M*-B distances decreases. Least for ZrB_{2-x}, more for NB_{2-x}, and most for MoB_{2-x}. This correlates well with the volume in Fig. 4(a).

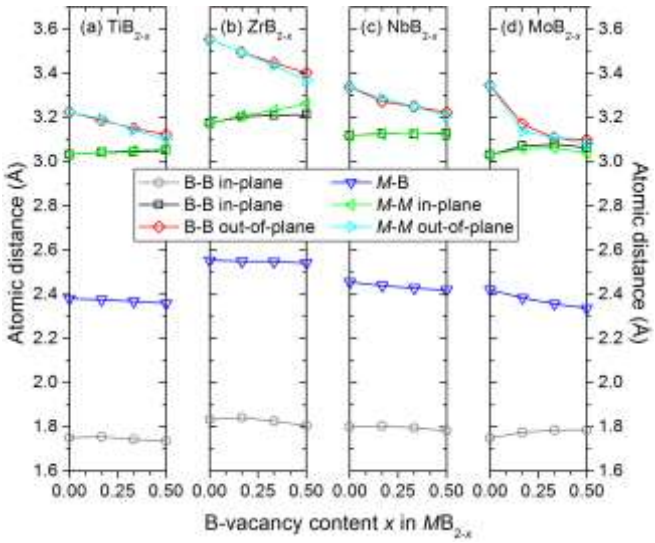

Figure 5. Average atomic distances for in- and out-of-plane B-B, in- and out-of-plane *M*-*M*, and *M*-B of MB_{2-x} where M = Ti, Zr, Nb, Mo and for x = 0 and at three selected B-vacancy concentrations, x = 0.167, 0.250, 0.500.

In Fig. 6(a) the bulk modulus B_0 of MB_{2-x} is shown as function of B-vacancy concentration x. A decrease in B_0 is seen for M from group IV and V with increasing x. For group VI, B_0 of

CrB_{2-x} is close to constant for $x < 0.167$ after which it start to decrease whereas B_0 of both MoB_{2-x} and WB_{2-x} decreases at small x, compared to $x = 0$, followed by a small increase up to $x = 0.25$ and 0.333, respectively, and then decreases at higher x. Recently, phonon calculations of WB_2, with AlB_2 structure, showed imaginary frequencies which indicates that it is dynamically unstable [41]. By modifying WB_2, either through creation of puckered B-layers ($R\bar{3}m$ or $P6_3/mmc$) or formation of B-vacancies, the imaginary frequencies are expected to disappear as well as stabilize the phase. Possible explanations to these trends are discussed below.

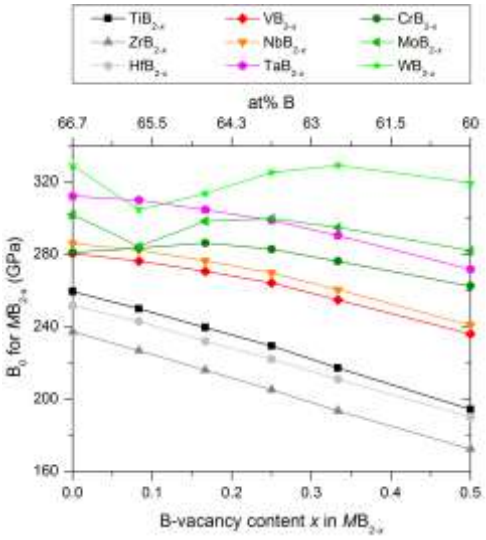

Figure 6. Bulk modulus B_0 as a function of B-vacancy concentration x in MB_{2-x} for M = Ti, Zr, Hf, V, Nb, Ta, Cr, Mo, W.

3.3. Electronic structure analysis

In Fig. 3 and 4, the change in stability and in the lattice parameters upon introduction of B-vacancies in MB_2 was demonstrated. The behavior within each group show similar trends with increasing B-vacancy concentration where MB_{2-x} in group IV are destabilized, i.e., TiB_2, ZrB_2, and HfB_2 are all line compounds, whereas MB_{2-x} with M from group V and VI show tendency for becoming stabilized with vacancy formation. Stabilization is also strengthened going from period 4 to 6 although not to an extent comparable to when going from Group IV to VI. To understand these trends, the electronic structure was evaluated for selected M in MB_{2-x}. Ti and Zr was chosen to represent change of period while Zr, Nb, and Mo represents change of group. The site projected and total density of states (PDOS and DOS) of MB_2 are shown in Fig. 7, where the vertical line indicates the Fermi level E_f. In general the DOS consists of three parts;

(i) the peak at low energies (~-14 to -8 eV) can mainly be attributed to localized B-2*s* electrons, (ii) around -5 eV, the bonding states of *M*-*d* and B-2*p* electrons can be found, and (iii) above the pseudo gap there are antibonding states dominated by *M*. From the DOS curves in panel (a) and (b), it is clear that TiB_2 and ZrB_2 have close resemblance. The Fermi level E_f is located in a valley, the so-called pseudogap, indicating that the bonding valence bands are completely filled. Such a feature is consistent with the higher chemical stability of TiB_2 and ZrB_2 as compared to other members of the metal diboride family. Going from Zr to Nb and Mo, the bonding peaks of *M*-*d* and B-2*p* are shifted towards lower energy due to an increased number of valence electrons. E_f is no longer located in the bottom of the pseudo gap, and is instead found in the region implying occupation of anti-bonding states, consistent with a predicted reduced stability evident from ΔH_{cp}= -435, -69, and +159 meV/atom for *M* = Zr, Nb, and Mo, respectively. WB_2, which belong to the same group as MoB_2, has also been demonstrated to have a large number of states at the Fermi level N(E_f) and filled anti-binding states just below E_f [42].

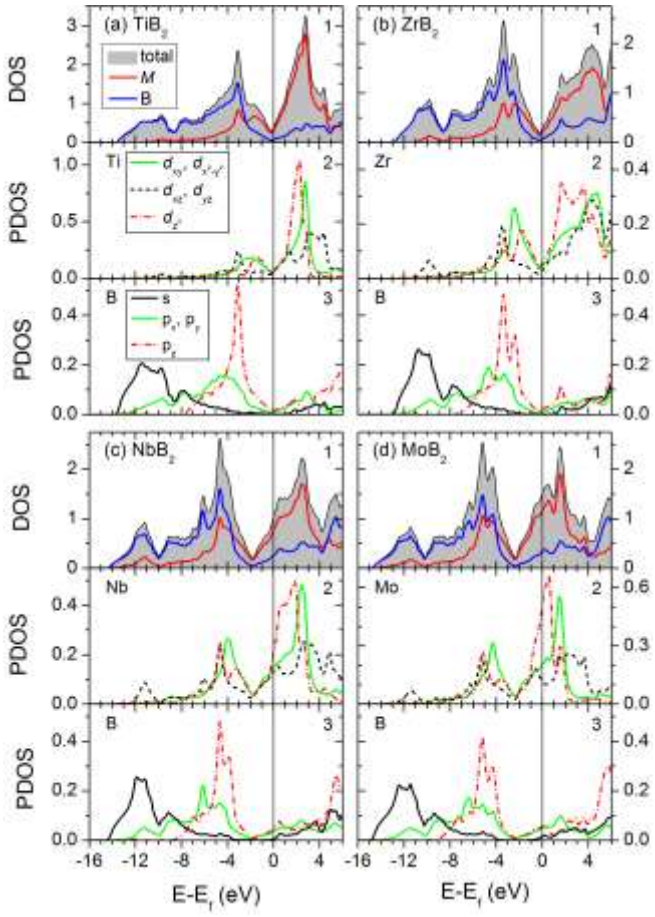

Figure 7. Total (1) and projected *M d* (2) and B *s* and *p* (3) density of states for MB_2 where *M* = Ti, Zr, Nb, and Mo. Vertical lines indicate the Fermi level E_f.

The influence of B-vacancies on the electronic structure in MB_2 are shown in panel (a) to (d) of Fig. 8 for selected B-vacancy concentration x. Fig. 8(e) shows the number of states at the Fermi level $N(E_f)$ as function of B-vacancy concentration x. First to note is that the introduction of vacancies, i.e. a decrease in electrons, does not fully follow a rigid-band approximation close to E_f. E.g., when Zr is replaced with Nb in Fig. 7, E_f is shifted upwards into the antibonding region with the overall shape of the DOS unchanged. However, when vacancies are created, both B-B and M-B bonds are broken which influence the electron density close to a vacancy and hence the electronic structure. This is most clear close to E_f where TiB_2 and ZrB_2 have an increase in $N(E_f)$ with increasing x but with a less distinct pseudo gap. Mind that the vacancies are distributed in a disordered manner. For NbB_2 and MoB_2 the overall shape of the DOS is close to unchanged upon introductions of B-vacancies and E_f is moved towards the minimum of the pseudo gap, with a decrease in $N(E_f)$ with increasing x as seen in Fig. 8(e). This is an indication that NbB_{2-x} and MoB_{2-x} are stabilized upon formation of vacancies, which is consistent with the calculated stability in Fig. 3. The observed change in $N(E_f)$ can mainly be attributed to M d states.

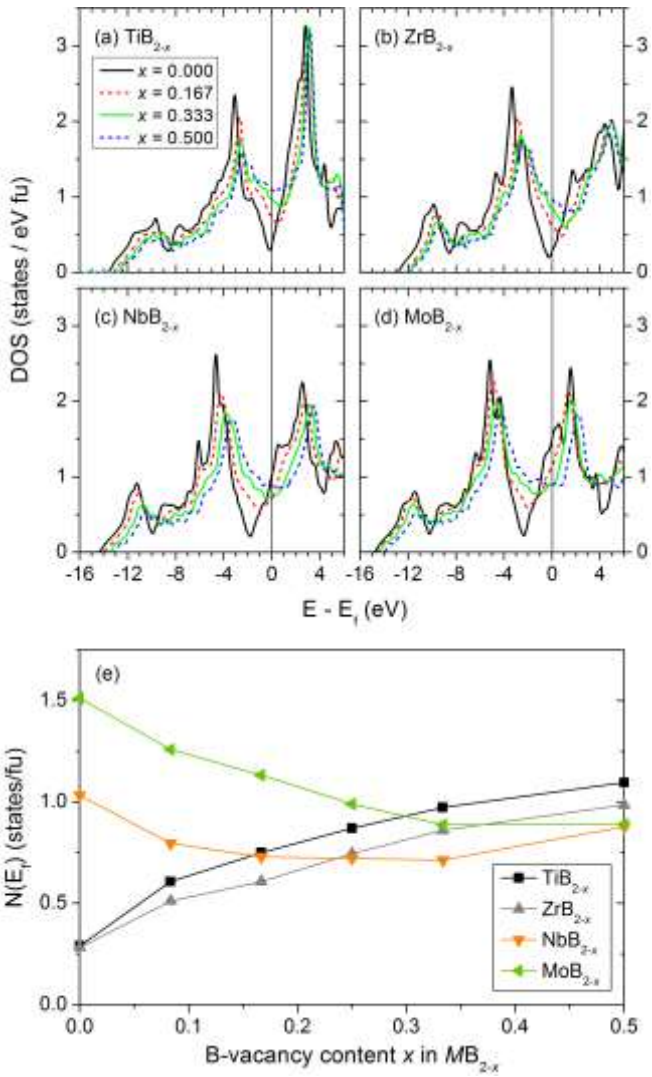

Figure 8. (a – d) Total density of states for MB_{2-x} where M = Ti, Zr, Nb, Mo at four selected B-vacancy concentrations. Vertical lines indicate the Fermi level E_f. In (e) the states at the Fermi level N(E_f) is given as function of the B-vacancy concentration x.

3.4. Bonding analysis

In order to examine the nearest-neighbor interactions of B-B, M-B, and M-M bonds, with their respective distance being shown in Fig. 5, the projected crystal orbital Hamiltonian population (pCOHP) curves were generated for MB_2 and $MB_{1.75}$ (x = 0.25). The results for M = Zr and Mo are shown in Fig. 9. For brevity, pCOHP of TiB_{2-x} and NbB_{2-x} are not shown, as the former displays large resemblance with ZrB_{2-x}, while the result for NbB_{2-x} are in between ZrB_{2-x} and MoB_{2-x}. In order to facilitate interpretation and to preserve the analogy to crystal orbital overlap population (COOP) analysis, results are here presented as –COHP, rather than COHP. From the COHP curves in Fig. 9(a) it is clear that B-B and B-Zr interactions are optimized in ZrB_2

with bonding orbitals completely filled and antibonding orbitals are empty. The B-B bonding is very strong with ICOHP = -4.09 eV/bond compared to B-Zr and Zr-Zr with ICOHP = -1.11 and -1.10 eV/bond. When B-vacancies are introduced in ZrB_2, antibonding orbitals becomes filled just below the E_f for the B-B interaction, resulting in a weakened bond with an average ICOHP = -3.94 eV/bond. For the B-Zr and Zr-Zr interactions the average ICOHP changes to -1.43 and -1.02 eV/bond, respectively.

From the pCOHP curves of MoB_2 in Fig. 9(b) the B-B and Mo-Mo interactions are optimized with filled bonding orbitals. Corresponding ICOHP = -4.33 and -1.05 eV/atom. The B-Mo interaction exhibit filled antibonding orbitals close to E_f (ICOHP = -1.16 eV/atom). For $MoB_{1.75}$ the B-B and Mo-Mo interactions are weakened, ICOHP = -3.70 and -0.92 eV/atom, with introduction of antibonding orbitals close to E_f for the latter and corresponding increase of their bond lengths as seen Fig. 5(d). Nonetheless, the COHP curve of the B-Mo interactions is optimized with bonding orbitals completely filled and antibonding orbitals empty, resulting in a significant strengthening of the bond to ICOHP = -1.79 eV/atom. This change can be related to the decreased B-Mo bond length seen in Fig. 5(d), and may explain why the bulk modulus is almost constant for $x \geq 0.25$ even though MoB_{2-x} shows the largest decrease in volume among the four MB_{2-x} phases considered. Such strengthening of the *M*-B is also found for NbB_{2-x}, although not as large as for MoB_{2-x}, with a resulting change in B_0 with increasing x in between that of ZrB_{2-x} and MoB_{2-x}.

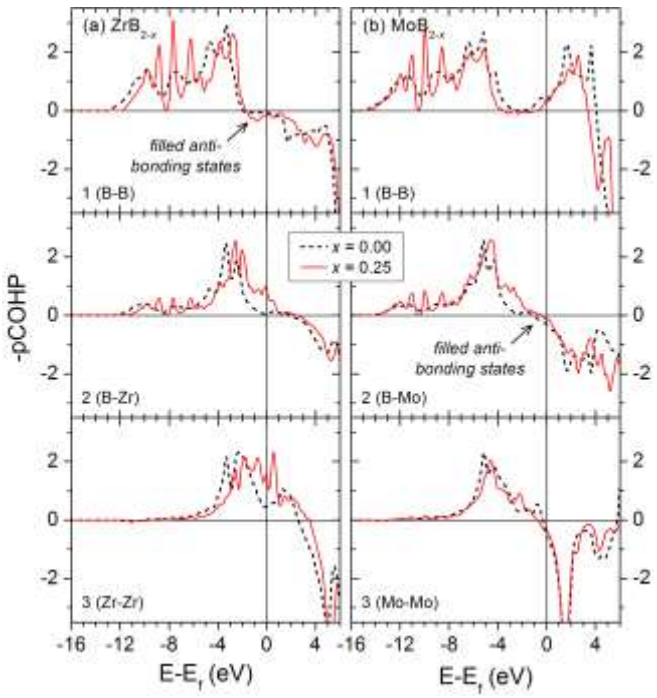

Figure 9. Projected crystal overlap Hamiltonian population (pCOHP) analysis for nearest neighbor B-B (1), B-*M* (2), *M*-*M* (3) bonds for MB_2 (dashed black lines) and $MB_{1.75}$ (solid red lines) where *M* = Zr and Mo. Vertical lines indicate the Fermi level E_f.

4. Conclusion

In conclusion, the phase stability, structural parameters, electronic structure, and bonding characteristics of MB_2 (*M* = Ti, Zr, Hf, V, Nb, Ta, Cr, Mo, W) upon B-vacancy formation have been investigated. NbB_2, TaB_2, CrB_2, MoB_2, and WB_2 are found to be stabilized when forming B-vacancies, which can be correlated to a decrease in the number of states at the Fermi level and by strengthening of the B-*M* interaction. This might explain why the bulk modulus for group VI is constant or increases with increasing B-vacancy concentration. For TiB_2, ZrB_2, and HfB_2 the introduction of B-vacancies have a destabilizing effect at least in part explained by the introduction of filled antibonding orbitals for the B-B interactions close to the Fermi level and an increase in states at the Fermi level. The results support the observations in magnetron sputtered Nb-B and Mo-B films, where hexagonal and substoichiometric NbB_{2-x} (x = 0.2) and MoB_{2-x} (x = 0.4) was formed [5, 7] and in bulk synthesis of hexagonal TaB_{2-x} (x = 0.19) [30].

Acknowledgements

The research was funded by the European Research Council under the European Community Seventh Framework Program (FP7/2007-2013)/ERC Grant agreement no [258509]. J. R. acknowledges funding from the KAW Fellowship program. Financial support from the Swedish Research Council (VR) is acknowledge by J. R., Grant No. 642-2013-8020 and 621-2012-4425, and by U. J., Grant No. 2014-5841. U. J. and J. R. also acknowledges funding from the Swedish Foundation of Strategic Research (SSF) Synergy Grant FUNCASE The simulations were carried out using supercomputer resources provided by the Swedish National Infrastructure for Computing (SNIC) at the National Supercomputer Centre (NSC) and the High Performance Computing Center North (HPC2N).

Appendix A

Table A1 shows calculated total energy and lattice parameters of MB_{2-x} where M = Ti, Zr, Hf, V, Nb, Ta, Cr, Mo, and W, for B-vacancy concentrations x = 0.00, 0.083, 0.167, 0.25, 0.333, and 0.50. Information related to prototypical structure, calculated lattice parameters and total energies for all competing phases included in this work are listed in Table A2.

Table A1. Calculated lattice parameters a and c, and total energy per formula unit for MB_{2-x} where M = Ti, Zr, Hf, V, Nb, Ta, Cr, Mo, and W. The prototype structure is AlB_2 (P6/*mmm*, 191).

M	x	a (Å)	c (Å)	E_0 (eV/fu)
Ti	0.000	3.033	3.229	-24.255
	0.083	3.040	3.205	-23.414
	0.167	3.046	3.190	-22.596
	0.250	3.054	3.167	-21.783
	0.333	3.056	3.146	-20.989
	0.500	3.074	3.107	-19.456
Zr	0.000	3.177	3.555	-24.879
	0.083	3.198	3.514	-24.044
	0.167	3.212	3.494	-23.241
	0.250	3.228	3.460	-22.449
	0.333	3.235	3.435	-21.674
	0.500	3.276	3.379	-20.174
Hf	0.000	3.145	3.490	-26.379
	0.083	3.163	3.448	-25.575
	0.167	3.177	3.432	-24.749
	0.250	3.189	3.399	-23.964
	0.333	3.196	3.375	-23.177
	0.500	3.233	3.323	-21.654
V	0.000	2.999	3.033	-24.687
	0.083	2.989	3.014	-24.061
	0.167	2.978	3.004	-23.385
	0.250	2.973	2.991	-22.705
	0.333	2.961	2.983	-21.989
	0.500	2.947	2.971	-20.535
Nb	0.000	3.119	3.339	-25.532
	0.083	3.127	3.297	-24.962
	0.167	3.123	3.278	-24.326
	0.250	3.127	3.260	-23.681
	0.333	3.124	3.243	-22.990
	0.500	3.131	3.212	-21.557
Ta	0.000	3.099	3.327	-27.181
	0.083	3.108	3.281	-26.660
	0.167	3.103	3.263	-26.067

	0.250	3.107	3.244	-25.459
	0.333	3.102	3.227	-24.833
	0.500	3.109	3.197	-23.417
Cr	0.000	2.981	2.940	-23.974
	0.083	2.973	2.899	-23.449
	0.167	2.957	2.878	-22.897
	0.250	2.944	2.864	-22.337
	0.333	2.919	2.866	-21.727
	0.500	2.873	2.870	-20.466
Mo	0.000	3.036	3.337	-25.031
	0.083	3.055	3.251	-24.530
	0.167	3.065	3.181	-24.001
	0.250	3.074	3.130	-23.490
	0.333	3.065	3.108	-22.933
	0.500	3.041	3.090	-21.752
W	0.000	3.017	3.367	-26.621
	0.083	3.050	3.274	-26.184
	0.167	3.054	3.202	-25.698
	0.250	3.062	3.147	-25.231
	0.333	3.056	3.116	-24.724
	0.500	3.035	3.091	-23.637

Table A2. Calculated equilibrium energy and lattice parameters for competing phases included in this work.

Phase	Prototype structure	Pearson symbol	Space group	*a* (Å)	*b* (Å)	*c* (Å)	E_0 (eV/fu)
Ti	Mg	hP2	$P6_3/mmc$ (194)	2.924		4.625	-7.762
Ti	Cu	cF4	$Fm\bar{3}m$ (225)	4.090			-7.706
Ti	W	cI2	$Im\bar{3}m$ (229)	3.236			-7.662
TiB_2	WB_2	hP12	$P6_3/mmc$ (194)	3.014		14.302	-23.063
TiB_2	MoB_2	hR18	$R\bar{3}m$ *h* (166)	3.018		21.386	-23.090
Ti_3B_4	Ta_3B_4	oI14	*Immm* (71)	3.038	3.261	13.741	-56.443
TiB	FeB	oP8	*Pnma* (62)	6.111	3.052	4.561	-16.079
TiB	NaCl	cF8	$Fm\bar{3}m$ (225)	4.530			-15.020
Ti_2B	$CuAl_2$	tI12	$I4/mcm$ (140)	5.650		4.732	-23.376
Zr	Mg	hP2	$P6_3/mmc$ (194)	3.239		5.182	-8.547
Zr	Cu	cF4	$Fm\bar{3}m$ (225)	4.537			-8.507
Zr	W	cI2	$Im\bar{3}m$ (229)	3.581			-8.467
ZrB_2	WB_2	hP12	$P6_3/mmc$ (194)	3.161		15.619	-23.552
ZrB_2	MoB_2	hR18	$R\bar{3}m$ *h* (166)	3.163		23.381	-23.572
ZrB_{12}	UB_{12}	cF52	$Fm\bar{3}m$ (225)	7.410			-91.443
ZrB	NaCl	cF8	$Fm\bar{3}m$ (225)	4.914			-15.976
Hf	Mg	hP2	$P6_3/mmc$ (194)	3.203		5.065	-9.955
Hf	Cu	cF4	$Fm\bar{3}m$ (225)	4.482			-9.883
Hf	W	cI2	$Im\bar{3}m$ (229)	3.543			-9.776
HfB_2	WB_2	hP12	$P6_3/mmc$ (194)	3.135		15.343	-25.110
HfB_2	MoB_2	hR18	R-3m h (166)	3.141		22.940	-25.137
HfB	NaCl	cF8	$Fm\bar{3}m$ (225)	4.839			-17.466
V	W	cI2	$Im\bar{3}m$ (229)	3.002			-9.116
V	Cu	cF4	$Fm\bar{3}m$ (225)	3.823			-8.873
V	Mg	hP2	$P6_3/mmc$ (194)	2.616		4.695	-8.863
VB_2	WB_2	hP12	$P6_3/mmc$ (194)	2.942		13.438	-24.392
VB_2	MoB_2	hR18	$R\bar{3}m$ *h* (166)	2.941		20.166	-24.386
V_2B_3	V_2B_3	oS20	*Cmcm* (63)	3.042	18.435	2.983	-42.257
V_3B_4	Ta_3B_4	oI14	*Immm* (71)	2.980	3.047	13.225	-59.792
V_5B_6	V_5B_6	oS22	*Cmmm* (65)	2.979	21.250	3.050	-94.779
VB	TlI	oS8	*Cmcm* (63)	3.052	8.049	2.971	-17.492
V_3B_2	U_3Si_2	tP10	$P4/mbm$ (127)	5.734		3.021	-44.322
Nb	W	cI2	$Im\bar{3}m$ (229)	3.322			-10.092
Nb	Mg	hP2	$P6_3/mmc$ (194)	2.883		5.243	-9.796
Nb	Cu	cF4	$Fm\bar{3}m$ (225)	4.233			-9.771
NbB_2	WB_2	hP12	$P6_3/mmc$ (194)	3.065		14.733	-25.337
NbB_2	MoB_2	hR18	$R\bar{3}m$ *h* (166)	3.067		22.082	-25.323
Nb_2B_3	V_2B_3	oS20	*Cmcm* (63)	3.325	19.597	3.142	-43.973
Nb_3B_4	Ta_3B_4	oI14	*Immm* (71)	3.157	3.320	14.174	-62.346
Nb_5B_6	V_5B_6	oS22	*Cmmm* (65)	3.167	22.918	3.322	-98.980
NbB	TlI	oS8	*Cmcm* (63)	3.315	8.788	3.179	-18.317
Nb_3B_2	U_3Si_2	tP10	$P4/mbm$ (127)	6.236		3.312	-46.806
Ta	W	cI2	$Im\bar{3}m$ (229)	3.323			-11.852

TaB_2	WB_2	hP12	*P*6$_3$/*mmc* (194)	3.050		14.635	-27.225
TaB_2	MoB_2	hR18	*R*$\bar{3}$*m h* (166)	3.052		21.943	-27.208
Ta_3B_4	Ta_3B_4	oI14	*Immm* (71)	3.140	3.304	14.058	-67.740
TaB	TlI	oS8	*Cmcm* (63)	3.293	8.709	3.162	-20.187
Ta_3B_2	U_3Si_2	tP10	*P*4/*mbm* (127)	6.196		3.296	-52.370
Ta_2B	Al_2Cu	tI12	*I*4/*mcm* (140)	5.795		4.879	-32.016
Cr	W	cI2	*Im*$\bar{3}$*m* (229)	2.852			-9.630
Cr	Cu	cF4	*Fm*$\bar{3}$*m* (225)	3.626			-9.241
Cr	Mg	hP2	*P*6$_3$/*mmc* (194)	2.489		4.457	-9.230
CrB_4	CrB_4	oI10	*Immm* (71)	2.855	4.750	5.488	-37.875
CrB_2	WB_2	hP12	*P*6$_3$/*mmc* (194)	2.914		12.837	-24.259
CrB_2	MoB_2	hR18	*R*$\bar{3}$*m h* (166)	2.916		19.239	-24.255
Cr_3B_4	Ta_3B_4	oI14	*Immm* (71)	2.942	2.922	13.037	-58.868
CrB	TlI	oS8	*Cmcm* (63)	2.930	7.848	2.918	-17.365
Cr_5B_3	Cr_5B_3	tI32	*I*4/*mcm* (140)	5.441		9.963	-71.601
Cr_2B	Mg_2Cu	oF48	*Fddd* (70)	4.218	7.352	14.602	-27.090
Mo	W	cI2	*Im*$\bar{3}$*m* (229)	3.169			-10.850
Mo	Mg	hP2	*P*6$_3$/*mmc* (194)	4.012			-10.431
Mo	Cu	cF4	*Fm*$\bar{3}$*m* (225)	2.774		4.887	-10.414
MoB_3	$Mo_{0.8}B_3$	hP16	*P*6$_3$/*mmc* (194)	5.213		6.308	-32.114
Mo_2B_5	Mo_2B_5	hR21	*R*$\bar{3}$*m h* (166)	3.215		22.348	-54.585
MoB_2	WB_2	hP12	*P*6$_3$/*mmc* (194)	3.026		13.993	-25.502
MoB_2	MoB_2	hR18	*R*$\bar{3}$*m h* (166)	3.024		21.012	-25.507
MoB	TlI	oS8	*Cmcm* (63)	3.165	8.554	3.094	-18.505
MoB	MoB	tI16	*I*4$_1$/*amd* (141)	3.131		17.072	-18.527
Mo_3B_2	U_3Si_2	tP10	*P*4/*mbm* (127)	6.047		3.160	-47.755
Mo_2B	$CuAl_2$	tI12	*I*4/*mcm* (140)	5.561		4.785	-29.313
W	W	cI2	*Im*$\bar{3}$*m* (229)	3.172			-13.017
W	Cu	cF4	*Fm*$\bar{3}$*m* (225)	4.023			-12.524
WB_4	MoB_4	hP10	*P*6$_3$/*mmc* (194)	2.954		11.004	-40.930
W_2B_5	$W2B_5$	hR21	*R*$\bar{3}$*m h* (166)	3.096		21.374	-57.677
W_2B_5	WB_2	hP14	*P*6$_3$/*mmc* (194)	3.097		14.241	-57.610
WB_2	WB_2	hP12	*P*6$_3$/*mmc* (194)	3.018		14.041	-27.385
WB_2	MoB_2	hR18	*R*$\bar{3}$*m h* (166)	3.016		21.069	-27.403
WB	TlI	oS8	*Cmcm* (63)	3.175	8.497	3.100	-20.418
WB	MoB	tI16	*I*4$_1$/*amd* (141)	3.139		16.968	-20.446
W_2B	Al_2Cu	tI12	*I*4/*mcm* (140)	5.571		4.771	-33.520
W_2B	W_2B	tI12	*I*4/*m* (87)	5.582		4.755	-33.524
B	B	hR36	*R*$\bar{3}$*m* (166)	4.902	12.549	2.560	-6.678

References

[1] Vajeeston P, Ravindran P, Ravi C, Asokamani R 2001 *Phys Rev B* **63** 045115
[2] Alling B, Högberg H, Armiento R, Rosen J, Hultman L 2015 *Sci Rep* **5**
[3] Nunes CA, Kaczorowski D, Rogl P, Baldissera MR, Suzuki PA, Coelho GC, et al. 2005 *Acta Mater* **53** 3679
[4] Liao PK, Spear KE 1986 *Bulletin of Alloy Phase Diagrams* **7** 232
[5] Nedfors N, Tengstrand O, Lu J, Eklund P, Persson POÅ, Hultman L, et al. 2014 *Surf Coat Tech*
[6] Nedfors N, Primetzhofer D, Wang L, Lu J, Hultman L, Jansson U 2015 *Surf Coat Tech* **266** 167
[7] Malinowski 2015 *in manuscript*
[8] Zunger A, Wei SH, Ferreira LG, Bernard JE 1990 *Phys Rev Lett* **65** 353
[9] Abrikosov IA, Simak SI, Johansson B, Ruban AV, Skriver HL 1997 *Phys Rev B* **56** 9319
[10] Ruban AV, Abrikosov IA 2008 *Rep Prog Phys* **71** 046501
[11] Hayami W, Momozawa A, Otani S 2013 *Inorg Chem* **52** 7573
[12] Perdew JP, Burke K, Ernzerhof M 1996 *Phys Rev Lett* **77** 3865
[13] Blöchl PE 1994 *Phys Rev B* **50** 17953
[14] Kresse G, Hafner J 1993 *Phys Rev B* **48** 13115
[15] Kresse G, Hafner J 1994 *Phys Rev B* **49** 14251
[16] Monkhorst HJ, Pack JD 1976 *Phys Rev B* **13** 5188
[17] Funahashi S, Hamaguchi Y, Tanaka T, Bannai E 1977 *Solid State Commun* **23** 859
[18] Maintz S, Deringer VL, Tchougréeff AL, Dronskowski R 2013 *Journal of Computational Chemistry* **34** 2557
[19] Deringer VL, Tchougréeff AL, Dronskowski R 2011 *The Journal of Physical Chemistry A* **115** 5461
[20] Dronskowski R, Bloechl PE 1993 *The Journal of Physical Chemistry* **97** 8617
[21] Murray JL, Liao PK, E. SK. B-Ti (Boron-Titanium). In: Massalski TB, editor. Binary Alloy Phase Diagrams. II ed1990. p. 544.
[22] Okamoto H. B-Zr (Boron-Zirconium). In: Massalski TB, editor. Binary Alloy Phase Diagrams. II ed1990. p. 560.
[23] Okamoto H. B-Nb (Boron-Niobium). In: Massalski TB, editor. Binary Alloy Phase Diagrams. II ed1990. p. 505.
[24] Spear KE, Liao PK. B-Mo (Boron-Molybdenum). In: Massalski TB, editor. Binary Alloy Phase Diagrams. II ed1990. p. 502.
[25] Dahlqvist M, Alling B, Abrikosov IA, Rosén J 2010 *Phys Rev B* **81** 024111
[26] Dahlqvist M, Alling B, Rosén J 2010 *Phys Rev B* **81** 220102
[27] Ingason AS, Mockute A, Dahlqvist M, Magnus F, Olafsson S, Arnalds UB, et al. 2013 *Phys Rev Lett* **110** 195502 1
[28] Mockute A, Dahlqvist M, Emmerlich J, Hultman L, Schneider JM, Persson POÅ, et al. 2013 *Phys Rev B* **87** 094113
[29] Thore A, Dahlqvist M, Alling B, Rosén J 2014 *Comput Mater Sci* **91** 251
[30] Okada S, Kudou K, Higashi I, Lundström T 1993 *J Cryst Growth* **128** 1120
[31] Woods HP, Wawner FE, Jr., Fox BG 1966 *Science* **151** 75
[32] Aizawa T, Suehara S, Hishita S, Otani S, Arai M 2005 *Phys Rev B* **71** 165405
[33] Fokwa BPT, Misse PRN, Gilleßen M, Dronskowski R 2010 *J Alloys Compd* **489** 339
[34] Kalfagiannis N, Volonakis G, Tsetseris L, Logothetidis S 2011 *J Phys D: Appl Phys* **44** 385402
[35] Ordanyan SS, Boldin AA, Suvorov SS, Smirnov VV 2005 *Inorg Mater* **41** 232

[36] Takagiwa H, Nishibori E, Okada N, Takata M, Sakata M, Akimitsu J 2006 *Science and Technology of Advanced Materials* **7** 22
[37] Bsenko L, Lundström T 1974 *J Less-Common Met* **34** 273
[38] Karki AB, Gautreaux DP, Chan JY, Harrison N, Browne DA, Goodrich RG, et al. 2008 *J Phys Cond Matter* **20** 035209
[39] Bauer A, Regnat A, Blum CGF, Gottlieb-Schönmeyer S, Pedersen B, Meven M, et al. 2014 *Phys Rev B* **90** 064414
[40] Jiang C, Pei Z, Liu Y, Xiao J, Gong J, Sun C 2013 *physica status solidi (a)* **210** 1221
[41] Li Q, Zhou D, Zheng W, Ma Y, Chen C 2013 *Phys Rev Lett* **110** 136403
[42] Liang Y, Gou Y, Yuan X, Zhong Z, Zhang W 2013 *Chemical Physics Letters* **580** 48